

Dynamic origin of conical helix magnetization textures stabilized by Dzyaloshinskii-Moriya interaction

C. Ríos-Venegas^{1,*}, F. Brevis¹, R. A. Gallardo^{1,2} and P. Landeros^{1,2,†}

¹*Departamento de Física, Universidad Técnica Federico Santa María, Avenida España 1680, Valparaíso, Chile*

²*Center for the Development of Nanoscience and Nanotechnology (CEDENNA), 917-0124 Santiago, Chile*



(Received 15 February 2022; revised 27 April 2022; accepted 20 May 2022; published 13 June 2022)

Since the beginning of the century, the possibility of having chiral spin textures in magnetic materials has been the subject of intense scientific interest. Chiral spin textures have been observed experimentally and described theoretically, bearing potential applications associated with their topological nature. This work theoretically explores the formation of chiral magnetic order in ultrathin magnetic films, where the antisymmetric Dzyaloshinskii-Moriya interaction induces a conical helix magnetization. By minimizing the internal energy of the helix, a simple model predicts the nucleation field, the pitch vector, and the cone angle that characterize the ground-state magnetization texture. It is further demonstrated that the formation of the helical order is connected with the spin waves excited close to the instability of the field-polarized state. Namely, when an in-plane magnetic field is reduced from saturation, a second-order phase transition arises when the spin-wave frequency approaches zero at a critical point where the conical helix nucleates. Interestingly, the wave vector at which the frequency becomes zero matches the pitch vector of the conical helix texture. Thus the instability point of the magnonic excitations is associated with the spin texture, as if the softened spin-wave modes crystallize in the chiral magnetic film. A critical competition among the magnetostatic and the anisotropy field is also found which influences the orbit described by a dynamic magnetization, changing it from circular to elliptical.

DOI: [10.1103/PhysRevB.105.224403](https://doi.org/10.1103/PhysRevB.105.224403)

I. INTRODUCTION

Left or right-handedness, known as chirality, plays an essential role in the symmetry properties of nature at all length scales and manifests itself in many scientific areas [1–5]. In magnetic materials, chiral effects are induced by a breaking of the inversion symmetry, which has been observed in noncentrosymmetric crystals and ferromagnet/heavy-metal bilayers [6–9], where the short-range antisymmetric Dzyaloshinskii-Moriya interaction (DMI) is the primary source of such chiral features [10–14]. Nonetheless, in curvilinear magnetic shells [15–18], ferromagnetic bilayers [19–22], and magnetization-graded ferromagnetic films [23] the chiral effects can be induced by magnetostatic interactions. The magnetic excitations, or spin waves (SWs), are also influenced by the chiral interactions, where a notable nonreciprocity in frequency has been first observed in thin films with DMI [24–31]. Specifically, two counterpropagating waves exhibit different phases, amplitudes, and frequencies at the same wave vector strength. The study of spin waves in magnetic textures is an emerging and exciting discipline, since there are varied types of magnetic configurations, including those showing periodic patterns, such as the conical helix (CH) usually observed in systems with DMI [32–37]. The magnonic excitations in any periodic magnetic texture will be like those obtained in magnonic crystals, which are currently prepared alternating two magnetic materials or fabricating films with

arrays of regular structures. Thus the static and dynamic effects of chiral periodic magnetic configurations are of high scientific interest since they permit the implementation of reconfigurable magnonic crystals [38–41].

It has been well established by several experimental techniques that a variety of spin textures similar to conical and helical appear in chiral thin films with DMI [42–57]. Also, under specific temperature and magnetic field conditions, skyrmions and skyrmion arrays may be induced [58–64]. Early in the 1960s, Dzyaloshinskii theoretically studied a helicoidal magnetic structure in nonmetallic and metallic antiferromagnetic materials with antisymmetric exchange [42,43]. Then, in the 1970s, Ishikawa *et al.* [44] and Motoya *et al.* [45] carried out a high-resolution neutron diffraction investigation and a detailed NMR study in MnSi compounds, demonstrating the existence of helical spin order, whose rotation axis coincides with the field direction and whose period is independent of the applied field. They confirmed that such a helical spin structure may exist at zero field and that the magnetization reversal process is interpreted due to the transitions from helical to conical and from conical to the field-polarized state [44,45]. In the 1980s, Bak and Jensen explained the helical magnetic configurations observed for the cubic phases of MnSi and FeGe with the Dzyaloshinskii-Moriya (DM) coupling [32]. Moriya and Miyadai realized further theoretical studies [47], explaining that the antisymmetric exchange interaction could stabilize a helical spin texture with an extended wavelength λ . Already in the 1980s, short-period helical textures (≈ 30 nm) had been observed below the Curie temperature by polarized-neutron diffraction, emerging from the noncentrosymmetric B20 structure of FeCoSi [48]. Helical

*cristobal.riosv@sansano.usm.cl

†pedro.landeros@usm.cl

spin order in $\text{Fe}_{0.5}\text{Co}_{0.5}\text{Si}$ chiral magnets were later imaged in real space by Lorentz electron microscopy [50,51], finding a helix with $\lambda = 90$ nm at 38 K, supporting early theoretical works [32,33]. Then, advances in technologies allowed new mechanisms of observation of conical and helical magnetic states, like small-angle neutron scattering [34,35]. Lorentz electron microscopy [48,50,51,56,61,65,66], spin-polarized scanning tunneling microscopy [52,54], resonant x-ray scattering [55], polarized neutron reflectometry [67], small-angle electron scattering [57], and electrical spectroscopy [37]. Moreover, the helical-to-conical transition [44,45] is a well-established fact that has been observed in noncentrosymmetric crystals [37,56] and thin films [54,57,59].

In the past decade, the presence of spin-spiral structures has been experimentally confirmed in chiral magnets with bulk [39,52,68] and interfacial DMI [69–71]. As a result, cycloidal, helicoidal, conical, toroidal, among other magnetic textures, may be energetically favorable [41]. These textures appear due to the competition of different magnetic interactions. While symmetric Heisenberg exchange interaction aligns neighbor magnetic moments, the DMI favors a canted orientation. Therefore to study the chiral spin textures, a detailed analysis of the competition between Dzyaloshinskii-Moriya and other interactions, such as anisotropies, Zeeman, exchange, and the classical dipole-dipole interaction, is required. It is well known that the proper treatment of magnetostatics is a demanding task, and for such reasons, in most of the literature dipolar coupling is not usually considered in its nonlocal form, or it is neglected [32–35,42–57,72–74]. In Ref. [75], for instance, the dipolar interaction was approximated as an effective anisotropy field, well justified by the fact that the stray field can be expressed as a local energy contribution, which works well for an ultrathin film. In the ultrathin limit it has been argued that the dipolar interaction slightly modifies theoretical results [37,53,76,77]. Such interaction, which is treated correctly through the use of micromagnetic simulations [54,63,78–80], must be counted accurately due to significant effects on nanomagnets, which increase with thickness [15,17,20,81]. For instance, dipolar effects could destroy the DM spiral rotation in favor of a vortex formation [53] and could generate twisted skyrmions [82]. Thus a complete theoretical description of chiral magnetic textures must consider the nonlocal nature of the dipolar interaction.

The spin-wave spectrum in ferromagnetic materials is usually calculated at large bias fields, in a polarized (P) or saturated state. The SW frequency decreases until zero when reducing the field, where the uniform state becomes unstable. In this context it is known that there is a connection between the nucleation of the magnetic textures and the low-frequency SW modes [83–96], which have been used to indicate and characterize the formation of different magnetic phases. For instance, Leaf *et al.* correlated the dynamic behavior of the spin waves with the formation of stripe-domain patterns in thin films with uniaxial anisotropy [84]. By analyzing the wavelengths of the SWs close to the point where the frequency is zero, they demonstrate that such wavelengths are of the same order as the period of the stripe domains [84]. Montoncello *et al.* reported that an abrupt magnetization switching is accompanied by a soft magnetic mode with a symmetry that determines the onset of the reversal path [85].

More recently, micromagnetic simulations showed this transition in long stripes and elliptical dots with in-plane magnetization, where the DMI enables the detection of SW modes that would remain invisible without it [96]. Therefore the softening of the spin-wave modes (modes at frequencies near zero) can be used as an alternative route to characterize magnetic textures.

In this paper, the formation of magnetic textures in ultrathin films with a thickness comparable to the exchange length (≈ 5 nm) is theoretically studied by considering symmetric and antisymmetric forms of exchange interaction, Zeeman interaction, perpendicular surface anisotropy, and nonlocal dipolar coupling. A conical helix magnetization model allows the calculation of such energies, from which it is demonstrated that the saturated film undergoes a magnetic phase transition from the in-plane saturated state to a conical helix texture. The cone angle, pitch vector, and nucleation field are calculated and discussed. Static results are compared with the spin-wave dynamics at the onset of the transition between the polarized and the conical helix states, demonstrating a direct connection between static and dynamic magnetic properties. It is further shown that the delicate competition of surface anisotropy with magnetostatics may also lead to elliptical-helical order, where the out-of-plane magnetization can be favored over in-plane magnetization or vice versa.

II. CONICAL HELIX MAGNETIZATION TEXTURE

This section explains the theoretical methods and simulations, starting with Sec. II A that describes the conical helix magnetization model and its energy contributions. In Sec. II B the minimization process is presented, and Sec. II C introduces the micromagnetic simulations. The nucleation field as a function of the Dzyaloshinskii-Moriya constant D is also obtained and discussed in Sec. II D.

A. Magnetization model and total energy

It is well known that spatially modulated magnetic textures are stable in ferromagnetic films with DMI. If the external field strength H is lower than a critical (or nucleation) field H_c , the saturated state becomes unstable and a conical helix structure may be a possible magnetic configuration that minimizes the total energy. A CH-magnetization model permits the calculation of the equilibrium state when both the interfacial and bulk DM interactions are considered. By assuming that the magnetic field \mathbf{H} is applied along the in-plane y axis (see Fig. 1), the unitary magnetization vector is written as

$$\hat{m}(\mathbf{r}) = \begin{pmatrix} \sin(\mathbf{q} \cdot \mathbf{r}) \sin \theta \\ \cos \theta \\ \cos(\mathbf{q} \cdot \mathbf{r}) \sin \theta \end{pmatrix}. \quad (1)$$

Here, $\mathbf{q} = (q \sin \varphi_q, q \cos \varphi_q, 0)$ is the conical helix vector (or pitch vector), and φ_q is the in-plane angle measured between \mathbf{H} and \mathbf{q} . The orientation of the helix will depend on the kind of DMI (bulk or interfacial) of the film. Also, θ is the cone angle measured from the rotation axis y [see Fig. 1(d)].

Under the absence of dipolar interaction (the bulk limit case, for instance), the bulk DM interaction stabilizes a conical-helical texture with a pitch-vector magnitude $q_0 =$

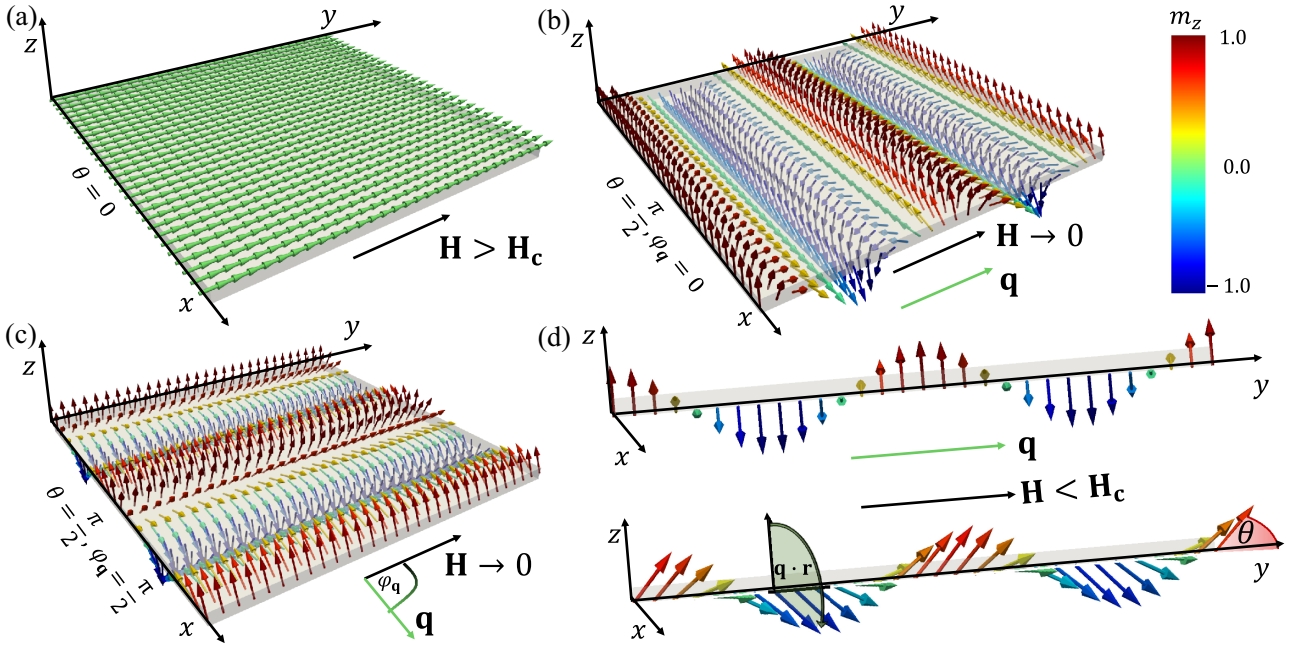


FIG. 1. Panel (a) represents the polarized state reached at sufficiently high magnetic fields $H > H_c$. The zero-field helical spin textures (with $\theta = \pi/2$) are stabilized by the (b) bulk and (c) interfacial Dzyaloshinskii-Moriya interaction. Here each film has a different direction of the pitch vector \mathbf{q} , while the external field along the y axis is reduced to zero. In (b) the propagation vector of the magnetization is parallel to \hat{y} (bulk DMI) and in (c) points along \hat{x} (interfacial DMI). Figure (d) illustrates the helical and conical states, where the angle θ is defined.

$D/2A$, where D is the DM strength and A is the exchange constant [39]. Nevertheless, dipole-dipole coupling plays an essential role in the magnetic properties in the ultrathin limit. Once the magnetic texture is formed, such a dipolar interaction favors the in-plane magnetization component to avoid the formation of magnetic charges at the top and bottom film surfaces. Hence, an elliptical-helical magnetization model must accurately describe the static properties. However, such a modification in the model depicted in Eq. (1) considerably complicates the calculations. Therefore a surface anisotropy is also considered in the calculations, which favors the out-of-plane component of the magnetization. Thus the current study considers the cases where the dipolar contribution and the surface anisotropy are more or less similar in magnitude, so the helix's ellipticity is not relevant. Besides, the proposed model assumes that the magnetization is uniform along the normal coordinate, as long as the film thickness d is comparable with the exchange length of the material, as is precisely the ultrathin case. Using Eq. (1), it is possible to calculate the total energy of the system,

$$E = E_{\text{ex}} + E_s + E_Z + E_{\text{dip}} + E_{\text{i,b-DM}}, \quad (2)$$

where E_{ex} is the exchange energy, E_s stand for the perpendicular surface anisotropy, E_Z is the Zeeman term, E_{dip} represents the dipolar energy, and the last term represents either the bulk ($E_{\text{b-DM}}$) or the interfacial ($E_{\text{i-DM}}$) DM energy. Explicit expressions of the calculated energies can be found in Appendix A.

The orientation of the pitch vector is determined by the kind of DMI (bulk or interfacial). Therefore angles that maximize the nonreciprocal effects are used (see Ref. [25]): $\varphi_{\mathbf{q}} = 0$ for bulk DMI and $\varphi_{\mathbf{q}} = \pi/2$ for interfacial DMI, which are oriented parallel and perpendicular to the applied field,

respectively. Such behavior is supported by the fact that the variation of the DM energy with $\varphi_{\mathbf{q}}$ is enormous as compared to that of the dipolar coupling or the surface anisotropy, whose variations are almost imperceptible. One must bear in mind that the current CH-magnetization model may not be adequate at the edges of a bounded film. Then, for the finite film case, it would be necessary to modify Eq. (1) to account for the canted spins at the boundaries and to include a phase angle to consider the spin rearrangement produced by the dipolar field inhomogeneity. Thus, results for ferromagnetic films with infinite lateral extension are presented in what follows, where the static CH model does not consider the edge contributions.

B. Energy minimization

By minimizing the total dimensionless energy $\epsilon = E/(\mu_0 M_s^2 V)$, concerning θ , the extreme condition $\partial \epsilon / \partial \theta = 0$ gives for bulk DMI,

$$\sin \theta \left[\frac{H}{M_s} + \cos \theta \left(\frac{2Aq^2}{\mu_0 M_s^2} - \frac{2Dq}{\mu_0 M_s^2} - \frac{K_{\perp}}{\mu_0 M_s^2} + \frac{1 - e^{-qd}}{2qd} \right) \right] = 0, \quad (3)$$

where V is the volume and M_s is the saturation magnetization. For interfacial DMI,

$$\sin \theta \left[\frac{H}{M_s} + \cos \theta \left(\frac{2Aq^2}{\mu_0 M_s^2} - \frac{2Dq}{\mu_0 M_s^2} - \frac{K_{\perp}}{\mu_0 M_s^2} + \frac{1}{2} \right) \right] = 0, \quad (4)$$

where three solutions are found: $\theta = 0, \pi$, and an intermediate angle $\theta(q)$. Here, $K_{\perp} = K_s/d$ is the volume-averaged surface anisotropy constant, with K_s being the surface anisotropy constant and d the thickness of the magnetic film. The behavior of

the cone angle θ , as a function of the external field and material parameters, can be obtained from the following expression for bulk DMI:

$$\theta(q) = \arccos \left(-\frac{H/M_s}{\frac{2Aq^2}{\mu_0 M_s^2} - \frac{2Dq}{\mu_0 M_s^2} - \frac{K_\perp}{\mu_0 M_s^2} + \frac{1-e^{-qd}}{2qd}} \right), \quad (5)$$

and for interfacial DMI,

$$\theta(q) = \arccos \left(-\frac{H/M_s}{\frac{2Aq^2}{\mu_0 M_s^2} - \frac{2Dq}{\mu_0 M_s^2} - \frac{K_\perp}{\mu_0 M_s^2} + \frac{1}{2}} \right). \quad (6)$$

For both types of DMI, the conical angle depends on q , H , D , and the other material parameters, and approach to $\pi/2$ when the field is zero. By increasing the external field, the conical angle decreases until it reaches zero at the nucleation field, which is discussed in Sec. II D.

The energy minimization analysis concerning q reveals that the energy minimum does not significantly change as the surface anisotropy constant K_\perp is modified (not shown). Similar behavior occurs for the pitch-vector dependence with the applied magnetic field. Nevertheless, the energy minimization shows a linear behavior of the pitch vector with the DM strength, in agreement with recent work [39]. This dependence is an expected result, since the DMI induces the magnetic texture and hence the conical helix profile is strongly dependent on it.

C. Micromagnetic simulations

To further explore the formation of the conical helix texture, micromagnetic simulations were performed using MUMAX3 [97]. The system consists of a 1-nm ultrathin film with DMI and lateral dimensions $1 \mu\text{m} \times 1 \mu\text{m}$ discretized into 1-nm side cells. Standard parameters for Permalloy (Py:Ni₈₀Fe₂₀) have been chosen: $M_s = 658 \text{ kA/m}$, $A = 11.1 \text{ pJ/m}$ (the same used in the analytical model), and an anisotropy constant $K_\perp = 0.272 \text{ MJ/m}^3$. Also, a 2-T field was applied to saturate the magnetization along the y axis. Then the external field was gradually reduced to permit the formation of the chiral texture. The process for bulk and interfacial-type DMI (with $D = 2.5 \text{ mJ/m}^2$) is shown in Fig. 2, where the instantaneous magnetization distribution for a central section of the film is presented for $H \gtrsim H_c$ [Figs. 2(a) and 2(c)], and $H < H_c$ [Figs. 2(b) and 2(d)], where $H \geq H_c$ corresponds to the polarized state (not shown). As expected for bulk DMI, the pitch vector in Figs. 2(a) and 2(b) is parallel to the field. In Figs. 2(c) and 2(d), the same values for the magnetic field are shown but for interfacial DMI, where $\mathbf{q} \perp \mathbf{H}$. An energy minimization algorithm was applied to obtain the most stable configuration between each field step. This process was performed for different values of the DM constant and perpendicular anisotropy. Results for the micromagnetic simulation are discussed and compared with the CH-magnetization model in Figs. 3 and 5.

D. Nucleation fields

The formation of the chiral texture is also understood by calculating the nucleation field, the field at which the equilibrium configuration starts to change. The magnetization saturates if H is larger than the nucleation (or critical) field

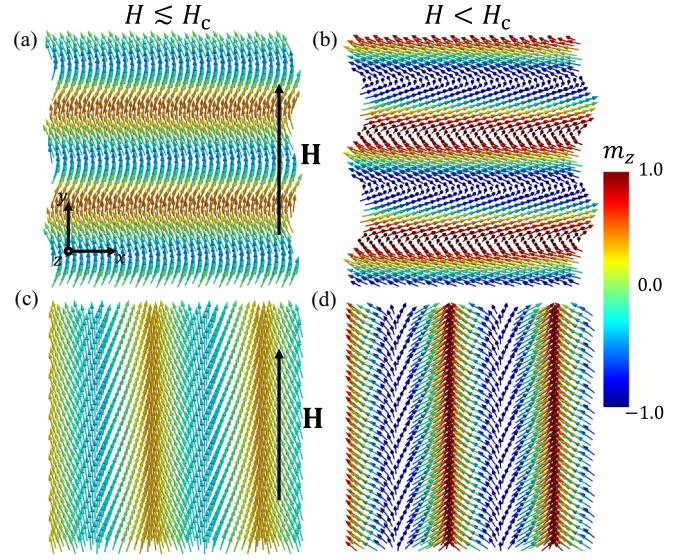


FIG. 2. Snapshots for the micromagnetic simulation showcasing the evolution of the conical helix texture stabilized by the bulk (a,b) and interfacial (c,d) Dzyaloshinskii-Moriya interactions. The conical helix texture is formed by reducing the applied magnetic field, with a particular orientation depending on the type of DMI. A piece of the infinite magnetic film is observed from the perpendicular z axis represented in Fig. 1, and the color code indicates the perpendicular component of the magnetization.

H_c , which means that $\theta = 0$ and $\hat{m} = \hat{y}$. By reducing the field from saturation, the magnetization is practically uniform until the nucleation field H_c is reached. At slightly lower fields, $H \lesssim H_c$, the nonuniform solution $\theta(q)$ arises, which represents a conical helix magnetic texture dependent on H and the material parameters. The other uniform solution occurs for a large opposite field, where $\theta = \pi$ and $\hat{m} = -\hat{y}$. The critical fields related to the magnetic phase transitions between the uniform state and the conical helix were analyzed, solving $\partial \epsilon^2 / \partial \theta^2 = 0$ for both types of DMI, at the polarized state solution, i.e., $\theta = 0$. For bulk-type DMI ($\varphi_q = 0$), the nucleation field for an infinite film is

$$\mu_0 H_c^{\text{b-DM}} = \frac{2D}{M_s} q - \frac{2A}{M_s} q^2 + \frac{K_\perp}{M_s} - \mu_0 M_s \frac{1 - e^{-qd}}{2qd}. \quad (7)$$

Also, for interfacial DMI ($\varphi_q = \pi/2$) the critical field is

$$\mu_0 H_c^{\text{i-DM}} = \frac{2D}{M_s} q - \frac{2A}{M_s} q^2 + \frac{K_\perp}{M_s} - \frac{\mu_0 M_s}{2}. \quad (8)$$

These nucleation fields depend explicitly on the pitch-vector magnitude, having a maximum at a critical value $q = q_c$. When the external field decreases until reaching the maximum of the nucleation field $H = H_c(q_c)$, the fully polarized state becomes unstable and the system starts to form a helical magnetization profile with a wavelength $\lambda_c = 2\pi/q_c$. Therefore it is verified that the critical value q_c that maximizes the nucleation field is effectively the pitch vector that minimizes the system's energy. The magnitude of the dipolar term [last term in Eq. (7)] for $qd = 0$ is $-\mu_0 M_s/2$. For nonzero q and d , the dipolar term decreases its absolute value in such a way that even for $d = 1 \text{ nm}$ there is an appreciable change of the dipolar term with q . Therefore, only on the limit $qd = 0$

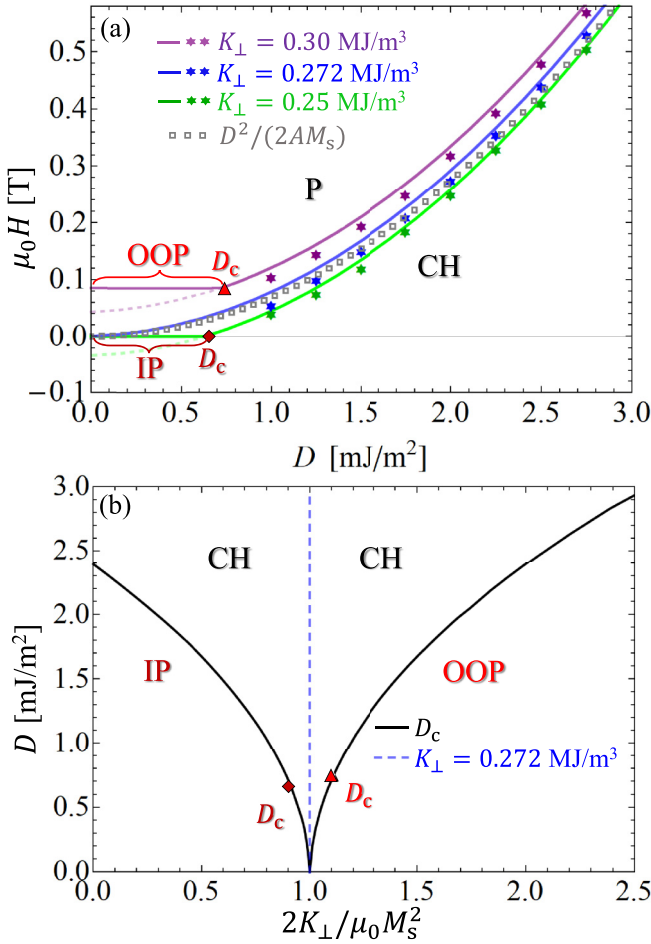


FIG. 3. Phase diagrams of the magnetic states for a thin film with bulk DMI, where P corresponds to the field-polarized state, and CH is the conical helix state. Here OOP (IP) represents the transition from the P state to an out-of-plane (in-plane) state, depicted by the red (maroon) line. (a) The nucleation fields from the calculations (simulations) are plotted by solid lines (filled stars) as a function of the DM strength for different anisotropy constants, where the green color denotes the case when the dipolar interaction is higher than the surface anisotropy. At the same time, blue symbolizes when both energies are similar in magnitude at $q = 0$, and the purple color symbolizes the situation when the surface anisotropy overcomes the dipolar interaction. The open squares indicate the analytical solution in the bulk limit [39]. Also, the critical DM strength D_c designates the critical value under which the nucleation field for coherent reversion (either IP or OOP) is larger than the critical field for the CH nucleation. In (b), D_c is calculated vs the ratio among the perpendicular anisotropy field with the demagnetizing field strength. The vertical dashed line represents the critical value $D_c = 0$ at which anisotropy and dipolar fields are equal at $q = 0$, that is, $K_\perp = \mu_0 M_s^2/2$.

the dipolar contribution is constant and able to be absorbed into the anisotropy. A slight change in the thickness may also alter the pitch vector q , because the subtle competition among anisotropy and magnetostatics depends on d . Then the balance between the dipolar and surface anisotropy is destroyed under the thickness increment, and the conical helix model will not describe the actual magnetic ground state. Instead, an elliptical-shaped helicoid should be appropriate for modeling the magnetization texture.

Figure 3(a) shows the calculated (solid lines) and simulated (filled stars) nucleation fields under which the conical helix texture begins to form as a function of the bulk DM strength. Three values of the anisotropy K_\perp were chosen, corresponding to a perpendicular anisotropy field ($\mu_0 H_\perp = 2K_\perp/M_s$) that is slightly lower (green), equal (blue), and scarcely higher (purple) than the dipolar field evaluated at $q = 0$ (equivalent to $\mu_0 M_s$). Note that the minor discrepancies between the model and MUMAX can be attributed to the edge effects in the simulations, where the spin deviations at the borders may influence the nucleation fields. Such deviations are not considered in the model established by Eq. (1). The case when dipolar interaction dominates and hence the magnetization prefers to remain in the film's plane is depicted by the green color in Fig. 3(a) ($K_\perp = 0.25$ MJ/m³). Here, $\mu_0 M_s > 2K_\perp/M_s$, and the nucleation field for the in-plane (IP) coherent rotation is higher than the CH nucleation field H_c^{b-DM} at $D < D_c$ (see IP zone). Such behavior means that there is a critical DM strength D_c (maroon diamond) above which the CH nucleates, while at $D < D_c$ the magnetization of the film reverses uniformly in the plane.

The blue data in Fig. 3(a) describes the case when dipolar and surface anisotropy are similar in magnitude so that they are canceled at $q = 0$. Hence the result for the critical field is similar to the analytical solution (see open squares) reported in Ref. [39], where $H_c^0 = D^2/(2A\mu_0 M_s)$. Such a result is valid in the bulk limit, where there are no surface magnetic charges, negligible dipolar energy, and the thickness dependence is irrelevant. The same result can be obtained from Eq. (7) in the bulk limit and by replacing the pitch vector by $q_0 = D/2A$. Nevertheless, as the constant D increases, both models (represented by the blue solid line and open squares) do not match exactly. The reason is associated with the fact that in the ultrathin limit, the dipolar energy depends slightly on qd and, even when the dipolar and surface anisotropy fields are canceled at $q = 0$, as q increases, the dipolar energy decreases so that $H_c^{b-DM} > H_c^0$. On the other hand, if the surface anisotropy interaction is more significant than the dipolar one [see purple data in Fig. 3(a)], the nucleation field for coherent out-of-plane (OOP) rotation H_c^{OOP} is higher than the CH critical field at $D < D_c$ (red triangle). Therefore, again there is a critical DM strength D_c above which the conical helix nucleates, but in this case, at $D < D_c$ the magnetization rotates uniformly and out of the plane due to the strong perpendicular surface anisotropy. Figure 3(b) shows the behavior of the critical DM strength, D_c , as a function of the ratio between the perpendicular anisotropy constant and the strength of the dipolar term at $q = 0$. The vertical dashed line represents the isotropic case $2K_\perp/M_s = \mu_0 M_s$, where $D_c = 0$. Above the solid black line, the CH texture is formed, while below it the coherent (either IP or OOP) magnetization rotation is preferred. Similar behavior is obtained for interfacial DMI (not shown).

III. SPIN-WAVE DYNAMICS

This section calculates the spin-wave dispersion at the saturated regime and discusses its connection with the magnetic texture. The DMI gives rise to nonreciprocal propagation of spin waves in chiral magnetic films [24,25]. For interfacial DM coupling, Damon-Eshbach (DE) modes ($\mathbf{M} \perp \mathbf{k}$) are

notoriously influenced by the DMI [26–29]. For the bulk-type DMI, experimental evidence shows that the nonreciprocity is mainly active in the backward-volume (BV) configuration ($\mathbf{M} \parallel \mathbf{k}$) [98–101]. These differences in both cases (DE and BV) are connected with the modulations observed in the conical helix ground state calculated previously because, for the interfacial DMI, the spin texture is ordered perpendicularly to the field axis (y). In contrast, for bulk DMI, the modulation of the helicoid is along the y axis. Therefore it is intriguing to analyze the spin waves close to the transition between the saturated and the conical helix states.

The SW dispersion for bulk [$f^{\text{b-DM}}(\mathbf{k})$] and interfacial [$f^{\text{i-DM}}(\mathbf{k})$] DMI, with in-plane magnetization, can be written as [25,29]

$$f^{\text{b-DM}}(\mathbf{k}) = \frac{\gamma D}{\pi M_s} k \cos \varphi_{\mathbf{k}} + \frac{\gamma}{2\pi} \sqrt{W_{xx}(\mathbf{k})W_{yy}(\mathbf{k})}$$

$$f^{\text{i-DM}}(\mathbf{k}) = \frac{\gamma D}{\pi M_s} k \sin \varphi_{\mathbf{k}} + \frac{\gamma}{2\pi} \sqrt{W_{xx}(\mathbf{k})W_{yy}(\mathbf{k})}, \quad (9)$$

where γ is the gyromagnetic ratio, k is the wave-vector magnitude, $\varphi_{\mathbf{k}}$ is the angle between the wave vector and the equilibrium magnetization, and the elements $W_{\alpha\alpha}(\mathbf{k})$ are associated with dipolar, exchange, Zeeman, and anisotropic interactions (see Appendix B). The SW dispersion, assuming a bulk DMI, is shown in Fig. 4, emphasizing the critical wave vector \mathbf{k}_c at which the frequency approaches zero, and the SWs become soft. Such a critical wave vector cannot be obtained analytically, even in the limit $kd \ll 1$, where a fourth-grade algebraic equation is obtained, but whose solutions are too long and not of practical use. Figure 4(a) shows the dispersion for different values of D , while Fig. 4(b) depicts the case for different values of the external field at $D = 1.653 \text{ mJ/m}^2$. In the latter case, one can note that the wave vector evaluated at the minimum of the SW dispersion does not depend on the external field. The k_c point defines the instability of the saturated state, appearing at only one propagation direction ($+\mathbf{k}$ or $-\mathbf{k}$, depending on the sign of D), evidencing the chiral nature of the magnonic system. Such features of the SW dynamics are directly connected with the conical helix spin structure, which also has chiral properties.

IV. CONNECTION BETWEEN STATICS AND DYNAMICS

Previous works argued that a specific spin-wave mode of the spectrum goes soft, triggering a local instability of the magnetization [84–87]. Below a threshold magnetic field, spin textures in ferromagnetic samples start to nucleate from the initially saturated state. Such a magnetic phase transition is usually accompanied by soft spin-wave modes at the critical point [91,92]. As the nucleation of the helical texture proceeds via the instability of the uniform magnetization state, it corresponds to a second-order phase transition, which contrasts with a first-order transition, where the field-polarized state becomes metastable and gradually depopulated [102].

The connection between the static and dynamic properties of the chiral system is shown in Fig. 5, where the nucleation field and the pitch vector are analyzed as a function of the Dzyaloshinskii-Moriya constant D . As before, the stars represent the pitch vector calculated from micromagnetic sim-

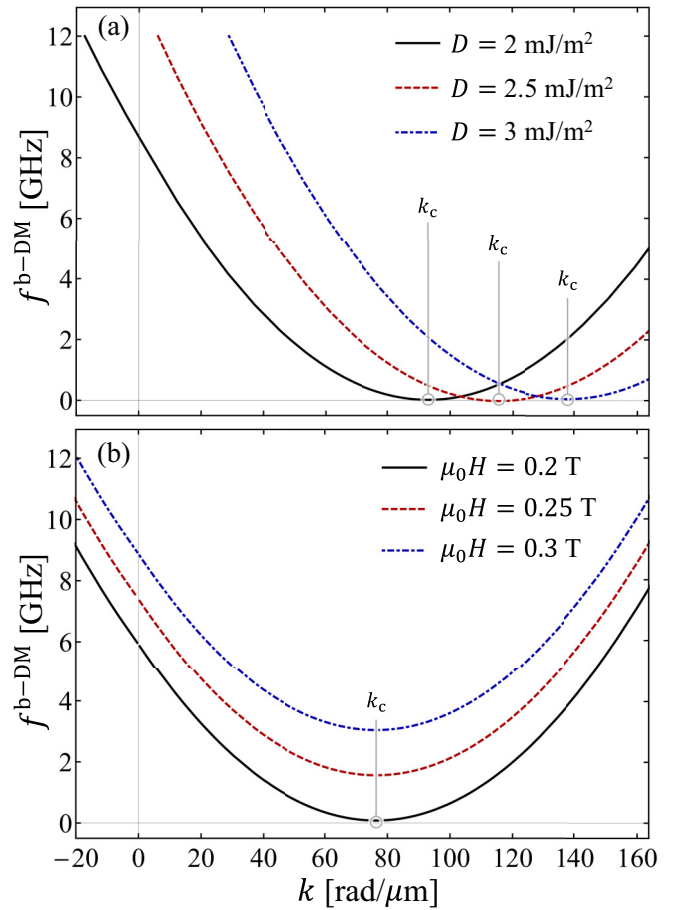


FIG. 4. Spin-wave dispersion relations calculated for a perpendicular anisotropy $K_{\perp} = 0.272 \text{ MJ/m}^3$. In (a), curves with different values of D are computed for different critical fields, and in (b), different external fields are considered for $D = 1.653 \text{ mJ/m}^2$. The magnonic dispersions are analyzed close to zero frequency, where the field-polarized state becomes unstable. The critical wave vector at which the spin waves soften is illustrated with vertical lines.

ulations. Figures 5(a) and 5(b) depict the critical field at which the CH spin texture nucleates (solid lines) and the field at which the spin waves soften [$f^{\text{b-DM}}(k_c) \rightarrow 0$]. Both critical fields match almost perfectly, which is expected because they describe the destabilization of the saturated state. In Figs. 5(c) and 5(d), the pitch vector q_c of the conical helix, and the critical wave vector k_c at which the SWs become soft, are compared. These critical wave vectors are analyzed against the DM constant, where the exchange-dominated pitch vector $q_0 = D/(2A)$ (dash line) of the bulk limit is also shown [39]. Overall, one can see that there is a wide range of D values where k_c matches with the q_c that minimizes the system's total energy at the nucleation field. The previous result allows connecting the dynamic and static features because when the saturated state becomes unstable, the magnetization forms a conical helix texture with a pitch vector (q_c) equals to the critical wave vector (k_c). Nevertheless, a slight difference between q_c and k_c appears at $D < D_c$.

To understand the discrepancies evidenced in Figs. 5(c) and 5(d) (for $D < D_c$), the orbits of the spin waves are analyzed at $k = k_c$ and $f^{\text{b-DM}}(k_c) \rightarrow 0$. The insets in

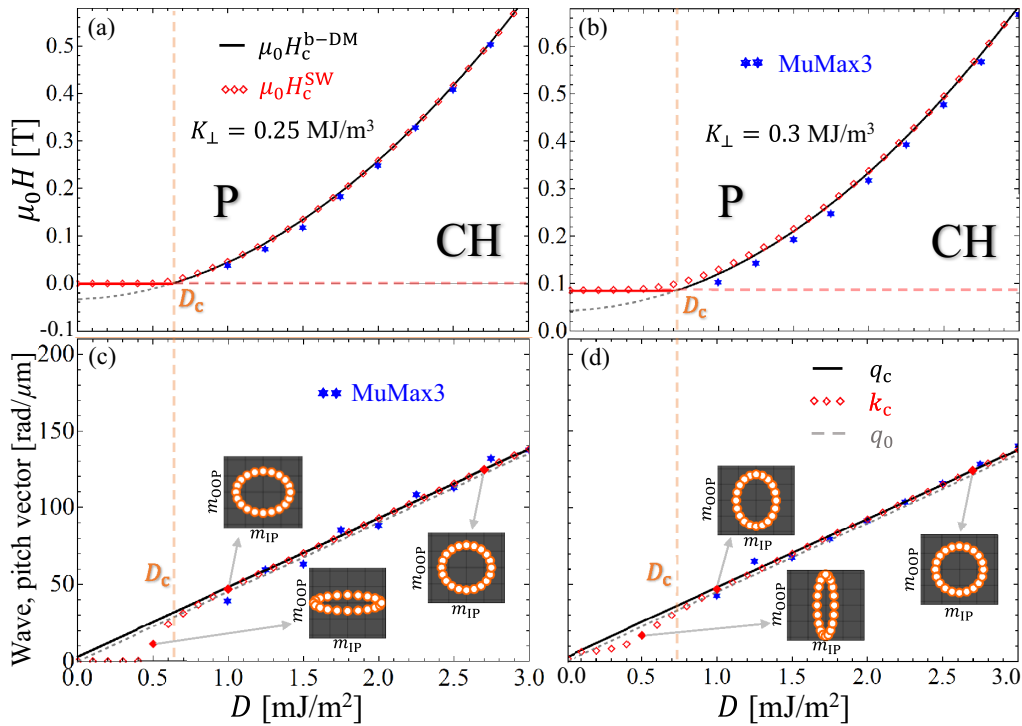


FIG. 5. Panels (a) and (b) show the critical fields for $d = 1$ nm obtained from both the conical helix magnetization model (lines) and the spin-wave dispersion (open symbols). The blue stars represent results from micromagnetic simulations. In (a, c) $K_{\perp} = 0.25$ MJ/m³ with a critical DM constant of $D_c = 0.64$ mJ/m², and in (b, d) $K_{\perp} = 0.3$ MJ/m³ with $D_c = 0.72$ mJ/m². In (c) and (d) the critical wave vector k_c at which the saturated state becomes unstable and the pitch q_c of the helix are compared. The gray dashed line corresponds to the bulk solution, $q_0 = D/2A$, found in the literature (when dipolar effects are not relevant), while red diamonds and black lines depict the k_c and q_c vectors, respectively. The insets in (c) and (d) show the orbits described by the dynamic magnetization components (in arbitrary units) evaluated at $k = k_c$ and $f^{b-DM}(k_c) \rightarrow 0$. The cases with $D = 0.5$ mJ/m², 1 mJ/m², and 2.7 mJ/m² have been used in the calculations of the orbits.

Figs. 5(c) and 5(d) show the orbits that describe the dynamic magnetization components, where it is easy to see that if the DM constant is lower than D_c , elliptical orbits are obtained. Depending on the competition between the perpendicular anisotropy and dipolar interactions, the elliptical shape has an in-plane major axis [Fig. 5(c)] or out-of-plane major axis [Fig. 5(d)]. Therefore, since the conical helix model describes a circular spin texture, it is not able to correctly represent the $D < D_c$ case, and hence a helicoidal state with elliptical magnetization texture is required to reproduce the behavior obtained from the SW dynamics, which is beyond the scope of this paper. Notice that in Fig. 5(c), for $D < 0.5$ mJ/m², the wave vector goes to zero, which means that the uniform mode is excited, while in Fig. 5(d), the wave vector is nonzero and a nonuniform mode is excited even for very low D . On the other side, as the DM constant increases, the SW orbit becomes more circular, and consequently, the conical helix pitch vector q_c and the wave vector k_c match. Note that even when the SW orbits are not entirely circular (see the orbits evaluated at $D = 1$ mJ/m²), the dynamic and static vectors (q_c and k_c) coincide nicely. Thus the relation between statics and dynamics allows for predicting some properties of the magnetic textures by using only the SW characteristics, since both the nucleation field and the pitch vector can be determined from the analysis of the SW spectra at $f^{b-DM}(k_c) \rightarrow 0$, where the soft spin waves seem to crystallize into a conical helix texture.

V. CONCLUSIONS

Chiral magnetic textures formed in thin films with Dzyaloshinskii-Moriya interactions have been studied theoretically and with micromagnetic simulations. A conical helix model is proposed, giving the nucleation fields, cone angle, and the pitch vectors that characterize the spin texture when interfacial or bulk Dzyaloshinskii-Moriya couplings are considered. The role of the perpendicular anisotropy and the dipolar interaction is also discussed. By comparing the nucleation fields for in-plane and out-of-plane coherent rotation with those corresponding to the conical helix formation, a critical Dzyaloshinskii-Moriya constant is derived, which depends on the film thickness and the competition among perpendicular anisotropy and the dipolar interaction. This critical DM strength separates the phase transitions based on a coherent magnetization rotation and a conical helix texture formation, evidencing the relevant role of perpendicular anisotropy and magnetostatics on ultrathin magnetic films, which can even turn the circular helix into an elliptical helix.

By analyzing the dynamic and static magnetic properties, it is demonstrated that the nucleation field and pitch vector can be directly obtained from the spin-wave examination, since its critical wave vector (evaluated at zero frequency) matches with the pitch vector associated with the conical helix texture. Therefore the formation of the spin textures induced by the Dzyaloshinskii-Moriya interaction can be understood

as a crystallization of soft spin waves, which can be used to characterize the imminent appearance of chiral magnetic order in thin films.

ACKNOWLEDGMENTS

The authors acknowledge financial support from Fondecyt through Grants No. 1201153 and No. 1210607, and the Basal Program for Centers of Excellence through Grant No. AFB180001 CEDENNA, CONICYT. Support from PIIC-USM and ANID PhD through Fellowship No. 2021-21211469 is also acknowledged.

APPENDIX A: TOTAL-ENERGY CALCULATION

In the following sections the different energy contributions are derived as a function of the helix parameters θ and q . A normalized total energy $\epsilon = E/(\mu_0 M_s^2 V)$ has been used in the calculations.

1. Exchange energy

The exchange energy in the micromagnetic continuum approximation is [103]

$$E_{\text{ex}} = \int_V \frac{A}{M_s^2} [(\nabla M_x)^2 + (\nabla M_y)^2 + (\nabla M_z)^2] dV. \quad (\text{A1})$$

Using the CH-magnetization model presented in Eq. (1), the exchange energy density becomes

$$\epsilon_{\text{ex}} = \frac{Aq^2}{\mu_0 M_s^2} \sin^2 \theta. \quad (\text{A2})$$

2. Perpendicular magnetic anisotropy

The energy associated with the surface perpendicular magnetic anisotropy is given by

$$E_s = - \int_S \frac{K_s}{M_s^2} (\mathbf{n} \cdot \mathbf{M})^2 dS, \quad (\text{A3})$$

where \mathbf{n} is the easy-axis (perpendicular to the film) direction, and $K_s > 0$ is the surface anisotropy constant. By using the relation $K_{\perp} = K_s/d$, the volume-averaged energy is

$$E_s = - \int_V \frac{K_{\perp}}{M_s^2} (\mathbf{n} \cdot \mathbf{M})^2 dV, \quad (\text{A4})$$

which is valid for ultrathin films. Then the resultant energy density for an infinite film is written as

$$\epsilon_s = - \frac{K_{\perp}}{2\mu_0 M_s^2} \sin^2 \theta. \quad (\text{A5})$$

3. Zeeman energy

The Zeeman energy is given by

$$E_Z = -\mu_0 \int_V \mathbf{M} \cdot \mathbf{H} dV, \quad (\text{A6})$$

where \mathbf{H} is the applied field. Then the energy density becomes

$$\epsilon_Z = - \frac{H}{M_s} \cos \theta. \quad (\text{A7})$$

4. Dipolar interaction

The dipolar field can be derived from Maxwell's equations, where $\mathbf{H}_{\text{dip}}(\mathbf{r}) = -\nabla \Phi_{\text{dip}}(\mathbf{r})$, with $\Phi_{\text{dip}}(\mathbf{r})$ the magnetostatic scalar potential given by

$$\nabla^2 \Phi_{\text{dip}}(\mathbf{r}) = \nabla \cdot \mathbf{M}(\mathbf{r}). \quad (\text{A8})$$

As the film thickness lies in the region $-d/2 < z < d/2$, a general expression can be calculated by assuming a homogeneous profile for the magnetization along with the thickness. Using the CH model [see Eq. (1)], it is obtained that $\nabla \cdot \mathbf{M}(x, y) = f(x, y)$, where

$$f(x, y) = M_s q \cos(qy \cos \varphi_q + qx \sin \varphi_q) \sin \theta \sin \varphi_q.$$

Then a particular solution of the magnetic potential is obtained which has the form [81]

$$\Phi_{\text{dip}}(\mathbf{r}) = \begin{cases} a_{\mathbf{q}} \sin \theta \cos(\mathbf{q} \cdot \mathbf{r}) e^{-qz}, & \text{if } z > d/2 \\ A_{\mathbf{q}} \sin \theta \cos(\mathbf{q} \cdot \mathbf{r}) e^{-qz} + B_{\mathbf{q}} \sin \theta \cos(\mathbf{q} \cdot \mathbf{r}) e^{qz} - \frac{f(x,y)}{q^2}, & \text{if } -d/2 \leq z \leq d/2 \\ b_{\mathbf{q}} \sin \theta \cos(\mathbf{q} \cdot \mathbf{r}) e^{qz}, & \text{if } z < -d/2. \end{cases} \quad (\text{A9})$$

The coefficients in Eq. (A9) can be determined from the boundary conditions at $z = \pm d/2$, from which it is found that

$$a_{\mathbf{q}} = \frac{A_{\mathbf{q}} q + B_{\mathbf{q}} e^{qd} q - e^{\frac{qd}{2}} M_s \sin \varphi_{\mathbf{q}}}{q}, \quad b_{\mathbf{q}} = \frac{B_{\mathbf{q}} q + A_{\mathbf{q}} e^{qd} q - e^{\frac{qd}{2}} M_s \sin \varphi_{\mathbf{q}}}{q}, \quad (\text{A10})$$

$$A_{\mathbf{q}} = M_s \frac{(\sin \varphi_{\mathbf{q}} - 1) e^{-\frac{qd}{2}}}{2q}, \quad B_{\mathbf{q}} = M_s \frac{(\sin \varphi_{\mathbf{q}} + 1) e^{-\frac{qd}{2}}}{2q}. \quad (\text{A11})$$

After some algebraic manipulations, the magnetic potential inside the film becomes

$$\Phi_{\text{dip}}(\mathbf{r}) = \frac{M_s}{2q} e^{-\frac{q(d+2z)}{2}} \cos(q[x \sin \varphi_{\mathbf{q}} + y \cos \varphi_{\mathbf{q}}]) (-1 + e^{2qz} + [1 + e^{2qz} - 2e^{\frac{q(d+2z)}{2}}] \sin \varphi_{\mathbf{q}}) \sin \theta. \quad (\text{A12})$$

Now, the dipolar field $\mathbf{H}_{\text{dip}} = -\nabla\Phi_{\text{dip}}(\mathbf{r})$ can be easily obtained, and the energy calculated from $E_{\text{dip}} = -\frac{\mu_0}{2} \int_V \mathbf{M} \cdot \mathbf{H}_{\text{dip}} dV$, which in the infinite film limit results in

$$\epsilon_{\text{dip}}(\varphi_{\mathbf{q}}) = \sin^2 \theta \frac{1 - e^{-qd} + \sin^2 \varphi_{\mathbf{q}}(e^{-qd} + qd - 1)}{4qd}, \quad (\text{A13})$$

while for $q = 0$,

$$\epsilon_{\text{dip}}(q = 0) = \frac{1}{4} \sin^2 \theta. \quad (\text{A14})$$

5. Bulk and interfacial Dzyaloshinskii-Moriya interactions

There are two basic types of inversion-symmetry-breaking mechanisms associated with the DMI [104], the noncentrosymmetric lattice (bulk DMI) and the one related to an interface (interfacial DMI). In the continuum limit, the energy for bulk DMI can be written as

$$E_{\text{b-DMI}} = -\frac{D}{M_s^2} \int_V \mathbf{M} \cdot (\nabla \times \mathbf{M}) dV,$$

where the energy density in the infinite film limit results in

$$\epsilon_{\text{b-DMI}} = -\frac{qD}{\mu_0 M_s^2} \cos \varphi_{\mathbf{q}} \sin^2 \theta. \quad (\text{A15})$$

On the other side, the interfacial DM energy term (with \hat{z} being the normal axis) can be written

$$E_{\text{i-DMI}} = -\frac{D}{M_s^2} \int_V [(\mathbf{M} \cdot \nabla) M_z - M_z (\nabla \cdot \mathbf{M})] dV,$$

and hence the energy density reads

$$\epsilon_{\text{i-DMI}} = -\frac{qD}{\mu_0 M_s^2} \sin \varphi_{\mathbf{q}} \sin^2 \theta. \quad (\text{A16})$$

APPENDIX B: SPIN-WAVE DISPERSION RELATION

The spin-wave dispersion relation for bulk and interfacial DMI can be obtained from Ref. [25]. For a ferromagnetic thin film with an in-plane magnetization, the $W_{\alpha\alpha}(\mathbf{k})$ elements used in Eq. (9) are

$$W_{xx}(\mathbf{k}) = W_{xx}(0) + \mu_0 M_s F(kd) \sin^2 \varphi_{\mathbf{k}} + \frac{2A}{M_s} k^2 \quad (\text{B1})$$

and

$$W_{yy}(\mathbf{k}) = W_{yy}(0) - \mu_0 M_s F(kd) + \frac{2A}{M_s} k^2, \quad (\text{B2})$$

where $W_{xx}(0) = \mu_0 H$, and $W_{yy}(0) = \mu_0 H + \mu_0 M_s - \frac{2K_{\perp}}{M_s}$. Here $F(x) = 1 - (1 - e^{-x})/x$, and $\varphi_{\mathbf{k}}$ is the angle between the magnetization and the wave vector \mathbf{k} .

-
- [1] S. Capozziello and A. Lattanzi, *Astrophys. Space Sci.* **301**, 189 (2006).
- [2] I. Dierking, *Symmetry* **6**, 444 (2014).
- [3] D. P. Glavin, A. S. Burton, J. E. Elsila, J. C. Aponte, and J. P. Dworkin, *Chem. Rev.* **120**, 4660 (2020).
- [4] S.-W. Cheong, D. Talbayev, V. Kiryukhin, and A. Saxena, *npj Quantum Mater.* **3**, 19 (2018).
- [5] Y. Tokura and N. Nagaosa, *Nat. Commun.* **9**, 3740 (2018).
- [6] A. N. Bogdanov and U. K. Röbber, *Phys. Rev. Lett.* **87**, 037203 (2001).
- [7] U. K. Röbber, A. N. Bogdanov, and C. Pfleiderer, *Nature (London)* **442**, 797 (2006).
- [8] N. Nagaosa and Y. Tokura, *Nat. Nanotechnol.* **8**, 899 (2013).
- [9] J. Chen, J. Hu, and H. Yu, *iScience* **23**, 101153 (2020).
- [10] I. Dzyaloshinsky, *J. Phys. Chem. Solids* **4**, 241 (1958).
- [11] T. Moriya, *Phys. Rev. Lett.* **4**, 228 (1960).
- [12] T. Moriya, *Phys. Rev.* **120**, 91 (1960).
- [13] A. Fert and P. M. Levy, *Phys. Rev. Lett.* **44**, 1538 (1980).
- [14] A. Fert, in *Metallic Multilayers*, Materials Science Forum Vol. 59 (Trans Tech Publications, Zurich, Switzerland, 1991), pp. 439–480.
- [15] P. Landeros and A. S. Núñez, *J. Appl. Phys.* **108**, 033917 (2010).
- [16] J. A. Otálora, M. Yan, H. Schultheiss, R. Hertel, and A. Kákay, *Phys. Rev. Lett.* **117**, 227203 (2016).
- [17] D. D. Sheka, O. V. Pylypovskyi, P. Landeros, Y. Gaididei, A. Kákay, and D. Makarov, *Commun. Phys.* **3**, 128 (2020).
- [18] R. A. Gallardo, P. Alvarado-Seguel, and P. Landeros, *Phys. Rev. B* **105**, 104435 (2022).
- [19] P. Grünberg, *J. Appl. Phys.* **57**, 3673 (1985).
- [20] R. A. Gallardo, T. Schneider, A. K. Chaurasiya, A. Oelschlägel, S. S. P. K. Arekapudi, A. Roldán-Molina, R. Hübner, K. Lenz, A. Barman, J. Fassbender, J. Lindner, O. Hellwig, and P. Landeros, *Phys. Rev. Applied* **12**, 034012 (2019).
- [21] V. Sluka, T. Schneider, R. A. Gallardo, A. Kákay, M. Weigand, T. Warnatz, R. Mattheis, A. Roldán-Molina, P. Landeros, V. Tiberkevich, A. Slavin, G. Schütz, A. Erbe, A. Deac, J. Lindner, J. Raabe, J. Fassbender, and S. Wintz, *Nat. Nanotechnol.* **14**, 328 (2019).
- [22] R. A. Gallardo, P. Alvarado-Seguel, A. Kákay, J. Lindner, and P. Landeros, *Phys. Rev. B* **104**, 174417 (2021).
- [23] R. A. Gallardo, P. Alvarado-Seguel, T. Schneider, C. Gonzalez-Fuentes, A. Roldán-Molina, K. Lenz, J. Lindner, and P. Landeros, *New J. Phys.* **21**, 033026 (2019).
- [24] R. L. Melcher, *Phys. Rev. Lett.* **30**, 125 (1973).
- [25] D. Cortés-Ortuño and P. Landeros, *J. Phys.: Condens. Matter* **25**, 156001 (2013).
- [26] K. Di, V. L. Zhang, H. S. Lim, S. C. Ng, M. H. Kuok, J. Yu, J. Yoon, X. Qiu, and H. Yang, *Phys. Rev. Lett.* **114**, 047201 (2015).
- [27] J. Cho, N.-H. Kim, S. Lee, J.-S. Kim, R. Lavrijsen, A. Solignac, Y. Yin, D.-S. Han, N. J. J. van Hoof, H. J. M. Swagten, B. Koopmans, and C.-Y. You, *Nat. Commun.* **6**, 7635 (2015).
- [28] S. Tacchi, R. E. Troncoso, M. Ahlberg, G. Gubbiotti, M. Madami, J. Åkerman, and P. Landeros, *Phys. Rev. Lett.* **118**, 147201 (2017).
- [29] R. A. Gallardo, D. Cortés-Ortuño, R. E. Troncoso, and P. Landeros, *Three-Dimensional Magnonics* (Jenny Stanford Publishing, Berlin, Heidelberg, 2019), pp. 121–160.

- [30] R. A. Gallardo, D. Cortés-Ortuño, T. Schneider, A. Roldán-Molina, F. Ma, R. E. Troncoso, K. Lenz, H. Fangohr, J. Lindner, and P. Landeros, *Phys. Rev. Lett.* **122**, 067204 (2019).
- [31] A. Barman, G. Gubbiotti, S. Ladak, A. O. Adeyeye, M. Krawczyk, J. Gräfe, C. Adelmann, S. Cotofana, A. Naemi, V. I. Vasyuchka, B. Hillebrands, S. A. Nikitov, H. Yu, D. Grundler, A. Sadovnikov, A. A. Grachev, S. E. Sheshukova, J.-Y. Duquesne, M. Marangolo, C. Gyorgy *et al.*, *J. Phys.: Condens. Matter* **33**, 413001 (2021).
- [32] P. Bak and M. H. Jensen, *J. Phys. C: Solid State Phys.* **13**, L881 (1980).
- [33] O. Nakanishi, A. Yanase, A. Hasegawa, and M. Kataoka, *Solid State Commun.* **35**, 995 (1980).
- [34] Y. Ishikawa and M. Arai, *J. Phys. Soc. Jpn.* **53**, 2726 (1984).
- [35] B. Lebech, P. Harris, J. Skov Pedersen, K. Mortensen, C. Gregory, N. Bernhoeft, M. Jermy, and S. Brown, *J. Magn. Magn. Mater.* **140-144**, 119 (1995).
- [36] M. Janoschek, F. Bernlochner, S. Dunsiger, C. Pfeleiderer, P. Böni, B. Roessli, P. Link, and A. Rosch, *Phys. Rev. B* **81**, 214436 (2010).
- [37] T. Schwarze, J. Waizner, M. Garst, A. Bauer, I. Stasinopoulos, H. Berger, C. Pfeleiderer, and D. Grundler, *Nat. Mater.* **14**, 478 (2015).
- [38] M. Kugler, G. Brandl, J. Waizner, M. Janoschek, R. Georgii, A. Bauer, K. Seemann, A. Rosch, C. Pfeleiderer, P. Böni, and M. Garst, *Phys. Rev. Lett.* **115**, 097203 (2015).
- [39] M. Garst, J. Waizner, and D. Grundler, *J. Phys. D: Appl. Phys.* **50**, 293002 (2017).
- [40] M. Weiler, A. Aqeel, M. Mostovoy, A. Leonov, S. Geprägs, R. Gross, H. Huebl, T. T. M. Palstra, and S. T. B. Goennenwein, *Phys. Rev. Lett.* **119**, 237204 (2017).
- [41] H. Yu, J. Xiao, and H. Schultheiss, *Phys. Rep.* **905**, 1 (2021).
- [42] I. E. Dzyaloshinskii, *Sov. Phys. JETP* **19**, 960 (1964).
- [43] I. Dzyaloshinskii, *Sov. Phys. JETP* **20**, 223 (1965).
- [44] Y. Ishikawa, K. Tajima, D. Bloch, and M. Roth, *Solid State Commun.* **19**, 525 (1976).
- [45] K. Motoya, H. Yasuoka, Y. Nakamura, and J. Wernick, *Solid State Commun.* **19**, 529 (1976).
- [46] K. Adachi, N. Achiwa, and M. Mekata, *J. Phys. Soc. Jpn.* **49**, 545 (1980).
- [47] T. Moriya and T. Miyadai, *Solid State Commun.* **42**, 209 (1982).
- [48] K. Ishimoto, Y. Yamaguchi, S. Mitsuda, M. Ishida, and Y. Endoh, *J. Magn. Magn. Mater.* **54-57**, 1003 (1986).
- [49] C. Pfeleiderer, D. Reznik, L. Pintschovius, H. von Löhneysen, M. Garst, and A. Rosch, *Nature (London)* **427**, 227 (2004).
- [50] M. Uchida, Y. Onose, Y. Matsui, and Y. Tokura, *Science* **311**, 359 (2006).
- [51] F. Nori and A. Tonomura, *Science* **311**, 344 (2006).
- [52] M. Bode, M. Heide, K. von Bergmann, P. Ferriani, S. Heinze, G. Bihlmayer, A. Kubetzka, O. Pietzsch, S. Blügel, and R. Wiesendanger, *Nature (London)* **447**, 190 (2007).
- [53] E. Y. Vedmedenko, L. Udvardi, P. Weinberger, and R. Wiesendanger, *Phys. Rev. B* **75**, 104431 (2007).
- [54] P. Ferriani, K. von Bergmann, E. Y. Vedmedenko, S. Heinze, M. Bode, M. Heide, G. Bihlmayer, S. Blügel, and R. Wiesendanger, *Phys. Rev. Lett.* **101**, 027201 (2008).
- [55] T. Frawley, R. Schoonmaker, S. H. Lee, C.-H. Du, P. Steadman, J. Stempfer, K. A. Ziq, S. J. Clark, T. Lancaster, and P. D. Hatton, *Phys. Rev. B* **95**, 064424 (2017).
- [56] K. Shibata, T. Tanigaki, T. Akashi, H. Shinada, K. Harada, K. Niitsu, D. Shindo, N. Kanazawa, Y. Tokura, and T.-h. Arima, *Nano Lett.* **18**, 929 (2018).
- [57] Y. Togawa, J. Kishine, P. A. Nosov, T. Koyama, G. W. Paterson, S. McVitie, Y. Kousaka, J. Akimitsu, M. Ogata, and A. S. Ovchinnikov, *Phys. Rev. Lett.* **122**, 017204 (2019).
- [58] A. N. Bogdanov and D. A. Yablonskii, *Sov. Phys. JETP* **68**, 101 (1989).
- [59] K. von Bergmann, S. Heinze, M. Bode, E. Y. Vedmedenko, G. Bihlmayer, S. Blügel, and R. Wiesendanger, *Phys. Rev. Lett.* **96**, 167203 (2006).
- [60] S. Mühlbauer, B. Binz, F. Jonietz, C. Pfeleiderer, A. Rosch, A. Neubauer, R. Georgii, and P. Böni, *Science* **323**, 915 (2009).
- [61] X. Z. Yu, Y. Onose, N. Kanazawa, J. H. Park, J. H. Han, Y. Matsui, N. Nagaosa, and Y. Tokura, *Nature (London)* **465**, 901 (2010).
- [62] S. Heinze, K. von Bergmann, M. Menzel, J. Brede, A. Kubetzka, R. Wiesendanger, G. Bihlmayer, and S. Blügel, *Nat. Phys.* **7**, 713 (2011).
- [63] M. T. Birch, D. Cortés-Ortuño, L. A. Turnbull, M. N. Wilson, F. Groß, N. Träger, A. Laurenson, N. Bukin, S. H. Moody, M. Weigand, G. Schütz, H. Popescu, R. Fan, P. Steadman, J. A. T. Verezhak, G. Balakrishnan, J. C. Loudon, A. C. Twitchett-Harrison, O. Hovorka, H. Fangohr *et al.*, *Nat. Commun.* **11**, 1726 (2020).
- [64] C. Back, V. Cros, H. Ebert, K. Everschor-Sitte, A. Fert, M. Garst, T. Ma, S. Mankovsky, T. L. Monchesky, M. Mostovoy, N. Nagaosa, S. S. P. Parkin, C. Pfeleiderer, N. Reyren, A. Rosch, Y. Taguchi, Y. Tokura, K. von Bergmann, and J. Zang, *J. Phys. D: Appl. Phys.* **53**, 363001 (2020).
- [65] W. Münzer, A. Neubauer, T. Adams, S. Mühlbauer, C. Franz, F. Jonietz, R. Georgii, P. Böni, B. Pedersen, M. Schmidt, A. Rosch, and C. Pfeleiderer, *Phys. Rev. B* **81**, 041203(R) (2010).
- [66] V. Simonet, M. Loire, and R. Ballou, *Eur. Phys. J.: Spec. Top.* **213**, 5 (2012).
- [67] N. A. Porter, C. S. Spencer, R. C. Temple, C. J. Kinane, T. R. Charlton, S. Langridge, and C. H. Marrows, *Phys. Rev. B* **92**, 144402 (2015).
- [68] M. N. Wilson, E. A. Karhu, D. P. Lake, A. S. Quigley, S. Meynell, A. N. Bogdanov, H. Fritzsche, U. K. Rößler, and T. L. Monchesky, *Phys. Rev. B* **88**, 214420 (2013).
- [69] G. Finocchio, F. Büttner, R. Tomasello, M. Carpentieri, and M. Kläui, *J. Phys. D: Appl. Phys.* **49**, 423001 (2016).
- [70] W. Kang, Y. Huang, X. Zhang, Y. Zhou, and W. Zhao, *Proc. IEEE* **104**, 2040 (2016).
- [71] L. Caretta, E. Rosenberg, F. Büttner, T. Fakhrol, P. Gargiani, S. Valvidares, Z. Chen, P. Reddy, D. Muller, C. Ross, and G. Beach, *Nat. Commun.* **11**, 1090 (2020).
- [72] A. B. Butenko, A. A. Leonov, U. K. Rößler, and A. N. Bogdanov, *Phys. Rev. B* **82**, 052403 (2010).
- [73] U. K. Rößler, A. A. Leonov, and A. N. Bogdanov, *J. Phys.: Conf. Ser.* **303**, 012105 (2011).
- [74] M. N. Wilson, A. B. Butenko, A. N. Bogdanov, and T. L. Monchesky, *Phys. Rev. B* **89**, 094411 (2014).
- [75] A. Leonov, T. Monchesky, N. Romming, A. Kubetzka, A. Bogdanov, and R. Wiesendanger, *New J. Phys.* **18**, 065003 (2016).
- [76] J. Kishine, K. Inoue, and Y. Yoshida, *Prog. Theor. Phys. Suppl.* **159**, 82 (2005).
- [77] S. Rohart and A. Thiaville, *Phys. Rev. B* **88**, 184422 (2013).

- [78] J. Mulkers, M. V. Milošević, and B. Van Waeyenberge, *Phys. Rev. B* **93**, 214405 (2016).
- [79] D. Cortés-Ortuño, M. Beg, V. Nehruji, L. Breth, R. Pepper, T. Kluyver, G. Downing, T. Hesjedal, P. Hatton, T. Lancaster, R. Hertel, O. Hovorka, and H. Fangohr, *New J. Phys.* **20**, 113015 (2018).
- [80] D. Cortés-Ortuño, N. Romming, M. Beg, K. von Bergmann, A. Kubetzka, O. Hovorka, H. Fangohr, and R. Wiesendanger, *Phys. Rev. B* **99**, 214408 (2019).
- [81] R. Arias and D. L. Mills, *Phys. Rev. B* **60**, 7395 (1999).
- [82] S. Castillo-Sepúlveda, R. Corona, A. Núñez, and D. Altbir, *J. Magn. Magn. Mater.* **484**, 451 (2019).
- [83] M. Bailleul, D. Olligs, and C. Fermon, *Phys. Rev. Lett.* **91**, 137204 (2003).
- [84] G. Leaf, H. Kaper, M. Yan, V. Novosad, P. Vavassori, R. E. Camley, and M. Grimsditch, *Phys. Rev. Lett.* **96**, 017201 (2006).
- [85] F. Montoncello, L. Giovannini, F. Nizzoli, P. Vavassori, M. Grimsditch, T. Ono, G. Gubbiotti, S. Tacchi, and G. Carlotti, *Phys. Rev. B* **76**, 024426 (2007).
- [86] F. Montoncello, L. Giovannini, F. Nizzoli, H. Tanigawa, T. Ono, G. Gubbiotti, M. Madami, S. Tacchi, and G. Carlotti, *Phys. Rev. B* **78**, 104421 (2008).
- [87] F. Montoncello, L. Giovannini, F. Nizzoli, P. Vavassori, and M. Grimsditch, *Phys. Rev. B* **77**, 214402 (2008).
- [88] F. G. Aliev, J. F. Sierra, A. A. Awad, G. N. Kakazei, D.-S. Han, S.-K. Kim, V. Metlushko, B. Ilic, and K. Y. Guslienko, *Phys. Rev. B* **79**, 174433 (2009).
- [89] H. Wilhelm, M. Baenitz, M. Schmidt, U. K. Röbler, A. A. Leonov, and A. N. Bogdanov, *Phys. Rev. Lett.* **107**, 127203 (2011).
- [90] M. Stebliy, A. Ognev, A. Samardak, L. Chebotkevich, R. Verba, G. Melkov, V. Tiberkevich, and A. Slavin, *J. Magn. Magn. Mater.* **384**, 166 (2015).
- [91] F. Montoncello, L. Giovannini, B. Farmer, and L. De Long, *J. Magn. Magn. Mater.* **423**, 158 (2017).
- [92] X. Zeng, G. Yang, and M. Yan, *Phys. B: Condens. Matter* **506**, 168 (2017).
- [93] M. Madami, G. Gubbiotti, S. Tacchi, and G. Carlotti, *J. Phys. D: Appl. Phys.* **50**, 453002 (2017).
- [94] J. Kindervater, I. Stasinopoulos, A. Bauer, F. X. Haslbeck, F. Rucker, A. Chacon, S. Mühlbauer, C. Franz, M. Garst, D. Grundler, and C. Pfleiderer, *Phys. Rev. X* **9**, 041059 (2019).
- [95] N. Mohanta, A. D. Christianson, S. Okamoto, and E. Dagotto, *Commun. Phys.* **3**, 229 (2020).
- [96] R. Silvani, M. Alunni, S. Tacchi, and G. Carlotti, *Appl. Sci.* **11**, 2929 (2021).
- [97] A. Vansteenkiste, J. Leliaert, M. Dvornik, M. Helsen, F. Garcia-Sanchez, and B. V. Waeyenberge, *AIP Adv.* **4**, 107133 (2014).
- [98] Y. Iguchi, S. Uemura, K. Ueno, and Y. Onose, *Phys. Rev. B* **92**, 184419 (2015).
- [99] S. V. Grigoriev, A. S. Sukhanov, E. V. Altynbaev, S.-A. Siegfried, A. Heinemann, P. Kizhe, and S. V. Maleyev, *Phys. Rev. B* **92**, 220415(R) (2015).
- [100] S. Seki, Y. Okamura, K. Kondou, K. Shibata, M. Kubota, R. Takagi, F. Kagawa, M. Kawasaki, G. Tatara, Y. Otani, and Y. Tokura, *Phys. Rev. B* **93**, 235131 (2016).
- [101] T. J. Sato, D. Okuyama, T. Hong, A. Kikkawa, Y. Taguchi, T.-h. Arima, and Y. Tokura, *Phys. Rev. B* **94**, 144420 (2016).
- [102] A. K. Suszka, A. Etxebarria, O. Idigoras, D. Cortés-Ortuño, P. Landeros, and A. Berger, *Appl. Phys. Lett.* **105**, 222402 (2014).
- [103] A. Aharoni, *Introduction to the Theory of Ferromagnetism* (Oxford University Press, Oxford, England, 2000).
- [104] A. Fert, V. Cros, and J. Sampaio, *Nat. Nanotechnol.* **8**, 152 (2013).